

## Equatorial Atmosphere Radar (EAR): System description and first results

Shoichiro Fukao, Hiroyuki Hashiguchi, Mamoru Yamamoto, Toshitaka Tsuda, Takuji Nakamura, and Masayuki K. Yamamoto

Radio Science Center for Space and Atmosphere, Kyoto University, Kyoto, Japan

Toru Sato

Graduate School of Informatics, Kyoto University, Kyoto, Japan

Masahiro Hagio and Yoshiyuki Yabugaki

Communication Systems Center, Mitsubishi Electric Corporation, Hyogo, Japan

Received 25 August 2002; revised 20 February 2003; accepted 19 March 2003; published 13 June 2003.

[1] A VHF Doppler radar with an active phased-array antenna system, called the Equatorial Atmosphere Radar (EAR), was established recently at the equator near Bukittinggi, West Sumatra, Indonesia ( $0.20^{\circ}\text{S}$ ,  $100.32^{\circ}\text{E}$ , 865 m above sea level). The EAR is a large monostatic radar which operates at 47.0 MHz with peak output power of 100 kW. The EAR uses a circular antenna array, approximately 110 m in diameter, which consists of 560 three-element Yagi antennas. Each antenna is driven by a solid-state transmitter-receiver module. This system configuration allows the antenna beam to be steered electronically up to 5,000 times per second. The scientific objective of the EAR is to advance knowledge of dynamical and electrodynamic coupling processes in the equatorial atmosphere from the near-surface region to the upper atmosphere. The equatorial atmosphere over Indonesia is considered to play an important role in global change of the Earth's atmosphere. This paper presents the system description of the EAR, including observational results of the equatorial atmosphere made for the first time with altitude resolution of 75–150 m. *INDEX TERMS*: 3360 Meteorology and Atmospheric Dynamics: Remote sensing; 3394 Meteorology and Atmospheric Dynamics: Instruments and techniques; 3374 Meteorology and Atmospheric Dynamics: Tropical meteorology; 3334 Meteorology and Atmospheric Dynamics: Middle atmosphere dynamics (0341, 0342); *KEYWORDS*: atmospheric radar, equatorial Indonesia, phased array

**Citation:** Fukao, S., H. Hashiguchi, M. Yamamoto, T. Tsuda, T. Nakamura, M. K. Yamamoto, T. Sato, M. Hagio, and Y. Yabugaki, Equatorial Atmosphere Radar (EAR): System description and first results, *Radio Sci.*, 38(3), 1053, doi:10.1029/2002RS002767, 2003.

### 1. Introduction

[2] The western Pacific region, called the Indonesian Archipelago, is a center of intense atmospheric motions closely associated with global atmospheric change. The world's most active convective clouds are generated in this region. The mechanisms responsible for these atmospheric changes and fluctuations, however, have not yet been clearly identified because of the sparseness of

observational data from that region. The mechanisms that cause atmospheric changes in the equatorial region are thought to have a hierarchical (or multiple) structure, one that would require observations of the atmosphere at different horizontal scales for comprehensive description [Nakazawa, 1988]. Ideally, it is necessary to conduct coordinated experiments that include various ground-based and space-based instruments to derive a comprehensive understanding of these mechanisms. To this end, we established the Equatorial Atmosphere Radar (EAR) at the equator near Bukittinggi, West Sumatra in the Republic of Indonesia ( $0.20^{\circ}\text{S}$ ,  $100.32^{\circ}\text{E}$ , 865 m above

sea level), in June 2001, to be a key ground-based facilities for these kinds of studies.

[3] Recently, efforts for networking atmospheric radars (reputable for their reliable and continuous operation) have been initiated by scientists from the United States of America (USA), France, Germany, Australia, Canada, and Japan. One such network near the equator is the Trans-Pacific Profiler Network (TPPN) operated by the U.S. National Oceanic and Atmospheric Administration (NOAA) [e.g., *Gage et al.*, 1991] since 1994. The original network consisted of six radars aligned along the Pacific equator from Piura, Peru in South America to Biak, Indonesia in the western Pacific. The radars at Piura and San Cristobal continuously operate today, although TPPN was closed in 2002. Similar but less sensitive radars are also operating in Thailand and Indonesia [e.g., *Hashiguchi et al.*, 1995]. However, coverage of the western Pacific region is not yet adequate for elucidating the mechanisms of atmospheric change. A few more radars are needed. The EAR is expected to be a key facility that will provide important complementary data.

[4] This paper presents a description of the EAR system and the first observational results obtained with the EAR. In Sections 2 and 3 we describe the EAR system design and details of the system configuration. A short description is given of its capability to perform frequency-domain interferometry in Section 4. In Section 5 we describe measurements of the antenna pattern obtained by using radio star emissions and Moon reflections as signal sources, and comparisons of wind profiles obtained by the EAR and radiosondes. In Section 6 we present initial observations of the EAR. Finally, we present our conclusions in Section 7.

## 2. System Design

[5] The EAR, a large-aperture Doppler radar for studying the equatorial atmosphere, is located at Bukit Kototabang, about 19 km to the north of Bukittinggi in West Sumatra, Indonesia (0.20°S, 100.32°E, 865 m above sea level). The EAR was designed to have the following capabilities: (1) ability to measure the tropospheric and lower stratospheric wind field up to 20 km altitude, (2) ability to steer the antenna beam on a pulse-to-pulse basis to any directions within 30° from zenith so that it can observe the detailed three-dimensional structure of small-scale processes in the equatorial atmosphere [e.g., *Worthington et al.*, 1999], (3) ability to measure altitude profiles of temperature by using the RASS (radio acoustic sounding system) technique [e.g., *Marshall et al.*, 1972; *Tsuda et al.*, 1994], (4) ability to observe the 3-m-scale (i.e., half the radar wavelength) field-aligned irregularities (FAIs) in the ionospheric *E* and *F* regions [*Fejer and Kelley*, 1980; *Fukao et al.*,

1988, 1991; *Yamamoto et al.*, 1991], (5) a single-pulse range resolution of 75 m, and even better accuracy for determining vertical displacement of thin atmospheric structures by using the frequency domain interferometry (FDI) technique [e.g., *Kudeki and Stitt*, 1987] or the frequency domain interferometric imaging (FII) technique [*Palmer et al.*, 1999; *Luce et al.*, 2001b], (6) a system recovery that is fast enough to obtain useful data at altitudes as low as 1.5 km, and (7) a facility optimized for ease of operation and maintenance because it will be installed at a remote site in West Sumatra, Indonesia.

[6] An active phased-array system, similar to that of the MU (middle and upper atmosphere) radar in Japan [*Fukao et al.*, 1985a, 1985b, 1990], was selected, based upon the established performance of the MU radar's fast beam steerability. In this kind of system phase shift and signal division and combination operations are carried out at low signal levels by electronic devices. Binary phase codes, such as Barker and complementary codes [e.g., *Schmidt et al.*, 1979; *Woodman*, 1980], are utilized for pulse compression techniques by which the signal-to-noise ratio can be improved without compromising range resolution. In addition to these two codes the EAR is able to use optimal complementary codes for decoding sampled data (Spano codes) [*Spano and Ghebrehbrhan*, 1996a, 1996b, 1996c]. Details of the EAR system, including several new inventions made for the EAR, are described in the following section.

## 3. System Configuration

[7] The EAR uses a quasi-circular antenna array with a diameter of approximately 110 m, which consists of 560 three-element Yagi antennas. It is an active phased-array system with each antenna driven by a solid-state transmitter-receiver module (TR module). With this system configuration the antenna beam can be steered electrically on a pulse-to-pulse basis by controlling phase shifters in the TR modules. The beam can be steered within 20  $\mu$ s, and up to 5,000 times per second. The EAR system is similar to the MU radar, built in Shigaraki, Japan in 1984 [*Fukao et al.*, 1985a, 1985b, 1990], but it implements a few new ideas and devices that have appeared in the last decade. In particular, efforts have been dedicated to modularize various subsystems and units by using commercial devices, where available.

[8] Table 1 shows the specifications of the EAR system. Its operating frequency is 47.0 MHz and its bandwidth is 4 MHz. The maximum peak and average radiation powers are 100 kW and 5 kW, respectively (the maximum duty ratio is 5%). A subpulse width as short as 0.5  $\mu$ s can be accommodated by the 4-MHz bandwidth of the system to satisfy the requirement for a maximum

**Table 1.** Specifications of the Equatorial Atmosphere Radar (EAR) System

Item	Specification
Location:	0.20°S, 100.32°E, 865 m above sea level
Geomagnetic latitude and longitude:	10.63°S, 171.93°E
Radar system:	Monostatic pulse Doppler radar
Operating frequency:	47.0 MHz
Antenna:	Quasi-circular antenna array of 560 three-element Yagi antennas
Aperture:	110 m in diameter
Beam width:	3.4° (half power width; one way)
Beam direction in azimuth:	0–360° in 0.1° steps
Beam zenith angle:	0–30° in 0.1° steps (no grating lobe)
Gain:	33 dBi
Transmitter	
Peak power:	100 kW (sum of all TR modules)
Average power:	5 kW (max; sum of all TR modules)
Number of TR modules:	560 units (same as Yagi antennas)
Single TR module's power:	180 W/unit
Pulse width:	0.5–256 μs
IPP:	200 μs-10 ms (variable in 200 μs steps)
Receiver	
Type:	Single super heterodyne
Noise figure:	5 dB (TR modules)
Pulse compression:	Barker, complementary and Spano codes (1 to 16 bits)
Subpulse width:	0.5, 1.0, 2.0, 4.0, 8.0, 16.0 μs (variable)
Dynamic range:	70 dB
A/D converter:	14 bits
Number of range gates:	256 (max.)

range resolution of 75 m. The nominal one way half power antenna beam width is 3.4°.

[9] The hardware of the EAR consists mainly of five subsystems; the antenna array (ANT), the transmitter and receiver (TRX), the signal modulator and demodulator (SMD), the signal processor (SP), and the host computer (HC). Figure 1 shows the schematic block diagram of the EAR system.

[10] The SMD generates a code-modulated RF signal, which is sent to the TRX for amplification to the specified power and radiated by the ANT into free space.

[11] The signal scattered from the atmosphere is received by the ANT, amplified by the TRX, and sent to the SMD. In the SMD the signal is detected and converted to a digital signal, which is subsequently sent to the SP for time-domain processing. The processed signal is then sent to HC for frequency-domain data processing to generate altitude profiles of wind velocity.

[12] The EAR system is connected to a backup electric power generator, which automatically starts to supply power within 1 min following a commercial power failure. Until electric power is available from the generator, the entire radar system, except for the TR

modules, is backed up by uninterruptible power supplies (UPSs).

### 3.1. Antenna Array (ANT)

[13] Figures 2 and 3 show views of the entire EAR antenna field and part of the Yagi array. The Yagi antennas are arrayed on grids of equilateral triangles with a side that is 4.5 m (approximately  $0.7\lambda$ :  $\lambda$  is wavelength) long, as shown in Figure 4. For this element spacing no grating lobe is formed at beam positions within 30° of zenith. The voltage standing wave ratio (VSWR) is less than 2.0.

[14] The array is divided for ease of signal distribution into 24 subarrays as shown in Figure 4. Each subarray, except for eight of those along the periphery in the north and south, consists of 24 antennas and an identical number of TR modules. Each of the eight subarrays along the periphery contains one to three fewer antennas (and TR modules) to produce a quasi-circular array pattern.

[15] The echoes returned from the atmosphere and ionosphere are received by the antennas and sent to the TR modules via duplexers (see Figure 5). The duplexer switching time is made less than 10 μs, which limits the closest range (1.5 km) from which data can be sampled and recorded. It is noted that the electromagnetic antenna near field effect prevents accurate observations with the

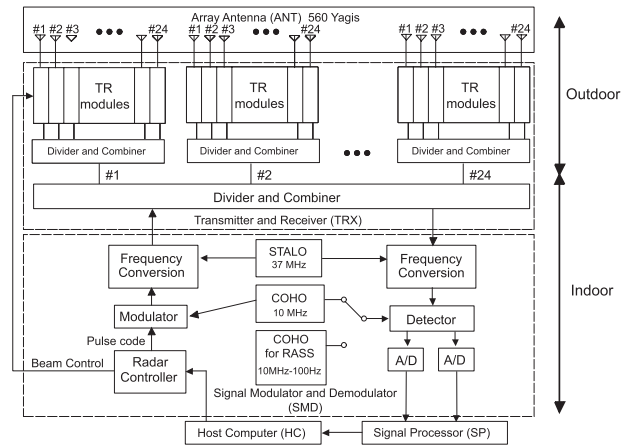


**Figure 1.** Schematic block diagram of the Equatorial Atmosphere Radar (EAR) system located at the equator near Bukittinggi, West Sumatra, Indonesia. The antenna array (ANT) and the transmitter and receiver (TRX) except for the indoor divider and combiner unit are installed in the antenna field. Other equipment is installed in the Observation House. STALO and COHO are abbreviations for stable local oscillator and coherent oscillator, respectively.



**Figure 2.** A view of the entire EAR.

EAR below 1.9 km altitude. Wind velocity measurements below the 1.5–2 km altitude are covered by an L-band boundary layer radar collocated at the EAR site [Renggono *et al.*, 2001].

[16] The antennas have a single linear polarization aligned in the north-south direction. Although use of linear polarization has the disadvantage of producing amplitude fading on signals propagated through the ionosphere because of Faraday rotation, it has no negative consequences for signals backscattered from the lower and middle atmosphere.

### 3.2. Transmitter and Receiver (TRX)

[17] A schematic block diagram of the TRX is shown in Figure 5. Each TR module is installed in a waterproof box that is mounted near the ground on the pole of its antenna (see Figure 3). The TRX is composed of a preamplifier (Pre-amp), an indoor divider and combiner unit (DCU), 24 outdoor DCUs, and 560 TR modules.

[18] For transmission, the RF (47.0-MHz) signal from the SMD is amplified by the Pre-amp and divided equally into 560 signals by the indoor and outdoor DCUs. Each of the 560 signals is sent at a low power level (0.3 mW or  $-5$  dBm) to a TR module and amplified to the final transmitting power level of 180 W (peak; 52.5 dBm). Figure 6 shows an example of the transmitted pulse with a 16-bit optimal code with a subpulse width of 1  $\mu$ s.

[19] During reception, the signal received from each antenna is amplified by a low-noise amplifier in each TR module, and the output signals from 560 TR modules are combined into one signal by the indoor and outdoor DCUs. The received signal is amplified further by the Pre-amp and sent to the SMD. The five-bit phase shifter in each TR module can change the phase in steps of  $11.25^\circ$  and provides the phase shifts required for both transmitted and received signals.

[20] The indoor DCU, which is installed within the Observation House, provides DC power and control signals to the outdoor DCUs and divides and combines

the RF signals. The outdoor DCUs are installed in the antenna field, and each unit supplies the RF signal, the DC power and control signals to 24 TR modules (or to 21 to 23 TR modules in the eight peripheral subarrays, as mentioned above). The 24 outdoor DCUs drive and control all of the TR modules.

[21] The TR module is composed of a driver amplifier, a power amplifier, a low-noise amplifier, an input duplexer, an output duplexer, a phase shifter for transmitted and received signals, a directional coupler for monitoring the transmitted power, and a control circuit for monitoring and controlling operations (Figure 5). The driver amplifier is a push-pull class AB power amplifier with a gain of 36.8 dB, while the power amplifier unit is composed of a two-stage push-pull class AB amplifier with a gain of 35.0 dB. The total loss due to insertion, filters, switches, and attenuators in a TR module is 14.3 dB. Therefore, the total effective gain becomes 57.5 dB. The Pre-amp is identical to a TR module.

[22] A photograph of a TR module is shown in Figure 7. Chassis dimensions are 37 cm  $\times$  55 cm  $\times$  24 cm (height, width and depth), and its weight is about 20 kg. The driver and high-power amplifiers are installed on the



**Figure 3.** Three-element Yagi antennas are shown, each with a transmitter-receiver module (TR modules) mounted, near the ground, on the pole.

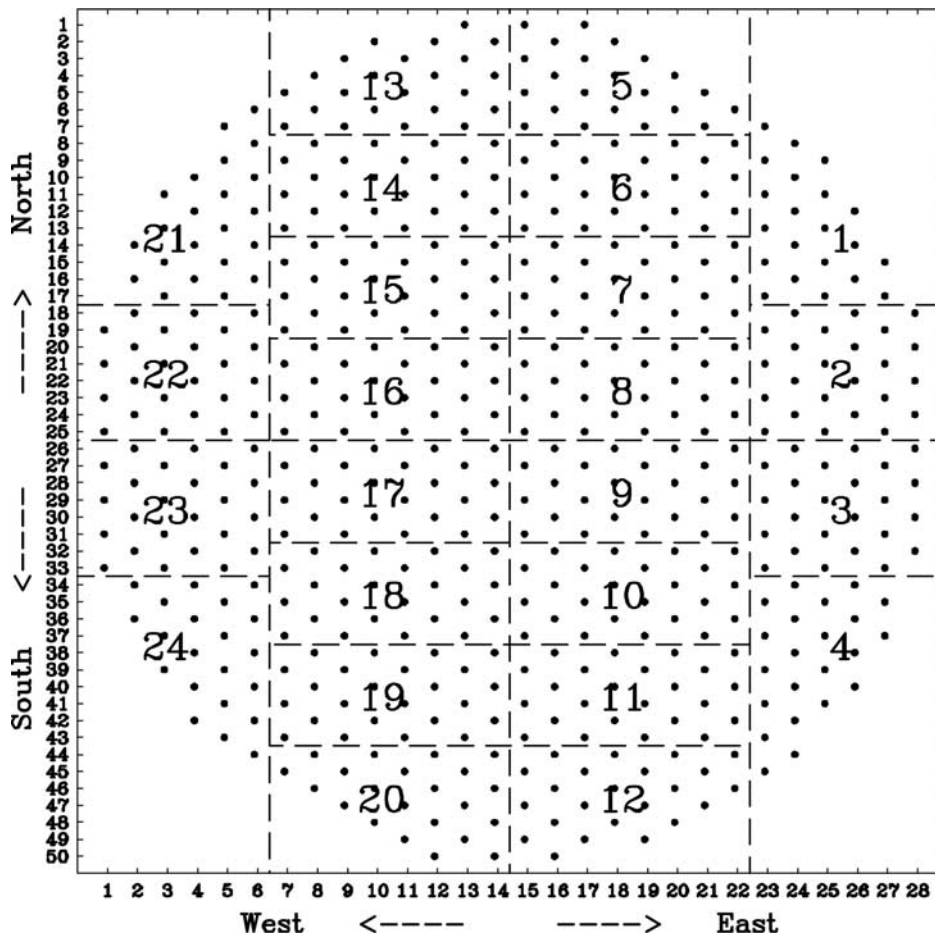


Figure 4. The EAR antenna array. Each dot represents the location of a three-element Yagi antenna and TR module.

right in Figure 7 while the output duplexer and low-pass filter are on the left top and the input duplexer and phase shifter are on the left bottom. A low-pass filter is inserted after the output duplexer to prevent transmission of harmonics (not shown in Figure 5). The mean time between failures (MTBF) of the TR modules is about 160,000 hours. This implies that approximately 30 TR modules need to be repaired every year. Each TR module continuously monitors its transmission power and sends a warning signal to the HC through the SP whenever the transmitting power drops.

[23] All cables leading from the indoor DCU to the balun of each antenna are physically of equal length. The balun is similar to the one used for the MU radar [Fukao *et al.*, 1985a]. The cable lengths between the indoor and outdoor DCUs, the outdoor DCU and TR module, and TR module and balun, are 150 m, 33 m and 2.7 m, respectively. The feed-cable loss that needs to be con-

sidered is 0.27 dB, which occurs between the TR module and the balun.

### 3.3. Signal Modulator and Demodulator (SMD)

[24] A schematic block diagram of the SMD is also shown in Figure 1. This subsystem is described briefly as follows: The SMD is composed of a stable local oscillator (STALO) of 37 MHz, a coherent oscillator (COHO) of 10 MHz, two frequency conversion units (one of which forms a super-heterodyne receiver), a phase detector, two analog-to-digital converters (A/Ds), and a radar controller (RC). The receiver noise level is -104 dBm, which is comparable to the minimum measured cosmic noise level of -103.6 dBm. This high noise level seems to be caused primarily by noise from the TRX and partly due to the low gain of the MDL. The receiver has a wide dynamic range of more than 70 dB.

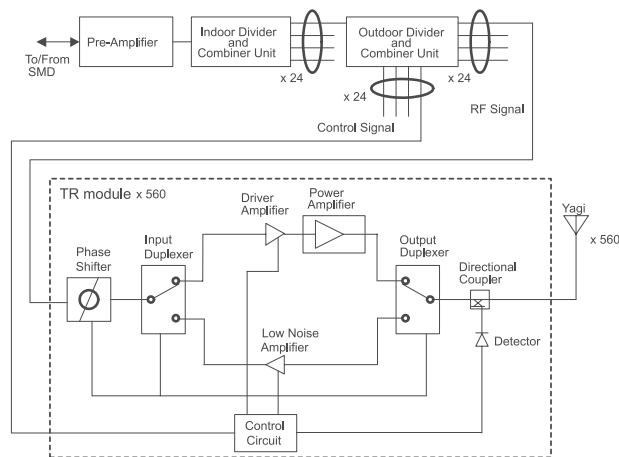


**Figure 5.** Schematic block diagram of the transmitter and receiver (TRX) of the EAR.

[25] The IF (intermediate frequency) transmitter source signal of 10 MHz is generated by applying a specified phase-modulation and pulse-modulation to the COHO signal in the modulator. The source signal is up-converted to the RF transmitted signal of 47.0 MHz by mixing it with the STALO signal in the frequency conversion unit. The RF signal is then sent to the TRX through a band-pass filter.

[26] The pulse width for transmission is determined by the subpulse width (0.5, 1.0, 2.0, 4.0, 8.0 or 16.0  $\mu\text{s}$ ) times the number of bits (1–16) used for phase modulation. The maximum pulse width available is 256  $\mu\text{s}$  (16  $\mu\text{s} \times 16$  bits). The IF band-pass filter is selected to match the subpulse width.

[27] The signal received at 47.0 MHz is down-converted to the IF of 10 MHz in the frequency conversion unit. The IF signal is subsequently down-converted to a video signal (analog signal) by the COHO and into in-phase (I) and quadrature-phase (Q) signals by a phase detector. In the case of the RASS mode the center frequency of the I and Q video signals is shifted 100 Hz below that of the normal mode (i.e., 10 MHz-100 Hz) in order to detect the acoustic line spectra. The I and Q video signals are then converted to 14-bit digital signals. The sampling interval is equal to the subpulse width. It is possible to delay the start of sampling by 1 to 1024 times the inter-pulse period (IPP) in order to receive Moon-reflection echoes for the purpose of antenna calibration (the delayed sampling mode).

[28] All timing signals for EAR operation are generated by the timing generator in the Radar Controller (RC). They are generated from the COHO signal of 10 MHz. The RC sends parameters of operation to the receiver and TRX.

[29] A GPS satellite receiver (not shown in Figure 1) receives the GPS time and reference signal. The RC utilizes this reference signal to synchronize the time counter to the GPS clock.

### 3.4. Signal Processor (SP)

[30] The SP performs a series of signal processing operations (pulse decoding, coherent integration, fast Fourier transform (FFT), incoherent integration), and sends the processed data to the host computer (HC). The interface between the SP and HC is a LAN 100 Base-T.

[31] A schematic diagram for the signal processing of the EAR is shown in Figure 8. The digitized I and Q signals are stored in the FIFO (First-In/First-Out) memory (double-buffered memory) in the A/D converters (see Figure 1). The output is sent to the pulse decoding and coherent integration units with header data added. Pulse decoding can be performed for any binary code with lengths up to 16 bits, such as Barker codes, ordinary complementary codes, and Spano codes [Spano and Ghebrebrhan, 1996a, 1996b, 1996c]. The maximum number of a code sequence is 32.

[32] After pulse decoding, the digitized I and Q signals are coherently integrated for each beam and range. The coherent integration unit adds a specified number of I and Q signals and outputs 32-bit data to double-buffered memory. The data from the ranges to be processed are selected and sent to the digital signal processing (DSP) unit.

[33] The integrated I and Q signals are stored in the buffered memory of the DSP unit, and rearranged into time series at respective ranges. The DSP then performs

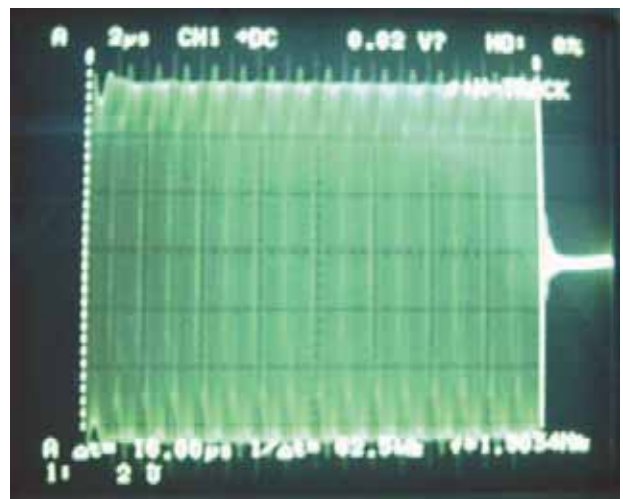


**Figure 6.** Photograph of the transmitted pulse with 16-bit optimal code and subpulse width of 1  $\mu\text{s}$ .



Figure 7. Photograph of the TR module.

complex FFT and power spectrum calculations on these time series. The computed power spectrum consists of 32-bit floating-point values. The DSP also performs a specified number of incoherent integrations of the power spectra. After incoherent integration the power spectra are sent to the HC via a 100 Base-T LAN interface. Time series of the digitized I and Q data (before FFT operation) can also be stored for specific off-line processings, such as frequency domain interferometric modes.

3.5. Host Computer (HC)

[34] The HC sends operating parameters to the RC and controls start/stop of operation of the entire system. The HC is a workstation having a CPU (Central Processing Unit) with 450 MHz clock and 512 MB main memory. The operating system is Solaris-UNIX. The observation software of the workstation has the following functions: (1) to set up observation parameters and to control the radar system, (2) to receive data from the SP, (3) to process data to estimate spectral parameters, (4) to record data on digital data storage (DDS) tapes, and (5) to display data graphically during observations.

[35] Observation software includes programs named "Observation Control," "Data Taking," "Signal Processing," "Tape Control," and "Quick Look." Observation Control sets up observation parameters to control observations. Data Taking sends radar control com-

mands to the RC and takes data from the SP through a 100 Base-T LAN interface. Signal Processing performs signal processing, such as the estimation of spectral parameters from data taken by the Data Taking program and the writing of results to hard disk. Tape Control transfers data stored on hard disk to DDS tape without interrupting observations. Quick Look is an on-line data-viewing program that reads data from the hard disk and plots them to the graphic display of the workstation. To control programs effectively, we use UNIX system calls

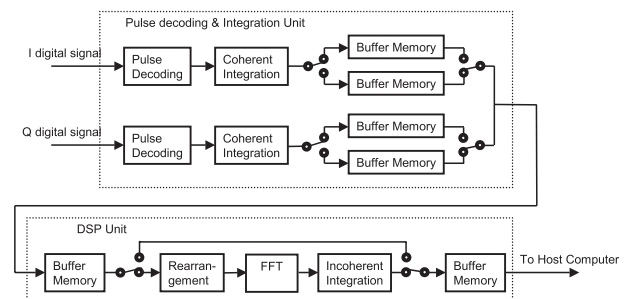


Figure 8. Schematic diagram of the signal processor (SP). The SP consists of two units: pulse decoding and integration unit and digital signal processing (DSP) unit.

such as “creation of process,” “semaphore,” and “shared memory.”

[36] The EAR system is under full supervision of the HC. The communication of the HC with the SP and RC is performed via a 100 Base-T LAN interface. Communications between the RC and each TR module are performed via RS-422 serial I/O interface. It takes less than 1 s to send the parameters to the RC and TR modules via the 100 Base-T LAN and serial interfaces. By utilizing this capability, the EAR can cyclically interleave the parameters (observation range, range (or altitude) resolution, time resolution, etc.) in such a short time and almost simultaneously observe, for instance, different altitude regions with different altitude and time resolutions most suitable to the respective regions. Sixteen different sets of observational parameters can be programmed within one cycle of observations.

#### 4. Frequency Domain Interferometry Capability

[37] Interferometric modes using multiple frequencies adjoining 47.0 MHz have been implemented to improve the accuracy of vertical displacement of thin structures in the atmosphere. These modes are particularly useful for investigations of thin turbulent or stable layers. Wave-induced instabilities that generate such thin structures are expected to be observed within the lower stratosphere in the equatorial atmosphere.

[38] For FDI (frequency domain interferometry) and FII (frequency domain interferometric imaging) observational modes four preselected frequencies, 47.0 MHz  $\pm$  250 kHz and 47.0 MHz  $\pm$  500 kHz, are transmitted on a pulse-to-pulse basis by changing the STALO frequency accordingly. These values lead to redundant frequency spacings but should be adequate for our objectives according to simulations and observations made by *Palmer et al.* [1999], *Luce et al.* [2001b], and *Smaini et al.* [2002]. The EAR is consequently capable of dual FDI observations with maximum frequency difference  $\Delta f = 1.0$  MHz and a minimum range resolution  $\Delta r = 150$  m, which represent an improvement by a factor of two (of both the initial resolution and frequency spacing used) over prior FDI observations at VHF. From observations using four frequencies different data processing schemes can be performed off-line, such as Fourier-based imaging, the Capon method [*Palmer et al.*, 1999; *Luce et al.*, 2001b], the Lagunas/Gasull method [*Smaini et al.*, 2002], and Singular Value Decomposition (SVD) with the MUSIC algorithm [*Luce et al.*, 2001b; *Smaini et al.*, 2002]. Preliminary results from the EAR data will be presented in a subsequent paper.

[39] Spatial-domain interferometry is not applicable because the EAR has only a single receiving channel available. The RASS capability [*Tsuda et al.*, 1994] has

also been applied effectively with the EAR; those results will be presented elsewhere.

### 5. Evaluation of Technical Reliability

[40] The EAR generally utilizes pulse-to-pulse beam steerability for its observations. It is necessary to confirm this capability by measuring the antenna pattern in operation. For this purpose, measurements of the antenna pattern have been made by using emissions from a radio star and radar reflections from the Moon. The performance concerned with measurements of wind profiles in the troposphere and lower stratosphere has been confirmed by comparisons with GPS radiosonde soundings.

#### 5.1. Radio Star Measurements for Receiving Antenna Pattern

[41] The antenna pattern in the receiving mode (without transmission) can be measured by using emissions from radio stars [e.g., *Guidice and Castelli*, 1971; *Czechowsky et al.*, 1984; *Fukao et al.*, 1985c]. We used Cygnus-A, which is the most intense point radio source detectable by the EAR and has a luminance temperature of 53,000 K at the EAR operating frequency of 47.0 MHz [*Maeda et al.*, 1999]. The proper steering of the antenna beam can be confirmed by determining the received power that maximizes at the expected time and zenith angle where the star crosses the meridian of the EAR.

[42] This kind of measurement was conducted between 0530 and 0640 LT on 25 April 2001. The beam was steered to eight different directions in 1.5° steps from 34.8° to 45.3° north of zenith. The northward beam at 40.8° zenith angle encountered Cygnus-A at 0607 LT. The antenna pattern approximately in the east-west direction can be measured by utilizing the Earth’s rotation. However, it is noted that absolute calibrations of directivity and gain are not allowed at this zenith angle, since grating lobes appear and deteriorate the radiation pattern significantly.

[43] Doppler spectra were calculated to remove intense interference which often entered the EAR bandwidth. Also, coherent integration was conducted to reduce the amount of data transferred from the SP to the HC, since the observations otherwise halted during the data transfer. Data were sampled at 128 points with 150-m interval, and coherent integration was performed 16 times. Then 256-point complex FFTs were calculated to obtain Doppler spectra every 6.6 s, which were averaged for approximately 20 s. The antenna gain was obtained in reference to the noise level of the resultant spectrum, and by plotting it versus time (or corresponding azimuth angle from the meridian).

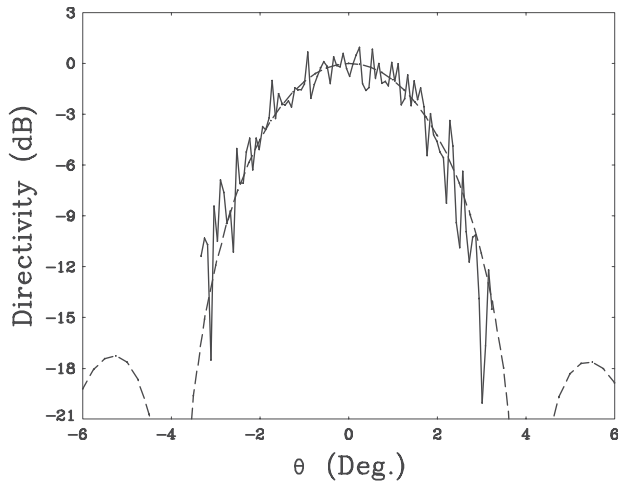


**Figure 9.** Relative gain of the EAR antenna pattern (solid curve) in receiving mode measured by using emission from the radio star Cygnus-A and the corresponding theoretical gain (dashed curve). The antenna beam is directed to  $40.8^\circ$  north of zenith.

[44] Figure 9 shows a cross section of the measured (solid curve) and theoretical (dashed curve) relative gains of the EAR approximately in the east-west direction. The measured directivity above  $-10$  dB is reliable. Both direction and gain measured for the main beam coincide well with the theoretical values. The antenna pattern in the north-south direction was measured by steering the antenna beam in the meridional plane and also found to be in good agreement with the theoretical pattern. Similar measurements were made using radiation from the Sun, but the measured pattern was occasionally more fluctuating than that obtained with Cygnus-A.

### 5.2. Moon Reflection Measurement for Total Antenna Pattern

[45] Since an ordinary antenna array has antenna patterns that are reciprocal for transmission (TX) and reception (RX), it is enough to measure the pattern in receiving mode only. On the other hand, the TX and RX patterns of an active phased array are, in general, not the same and are inseparably related to the distributed transmitter and receiver characteristics [Fukao *et al.*, 1985a, 1985c]. Therefore, it is necessary to measure the EAR antenna patterns by taking amplitude and phase characteristics of all TR modules into consideration. The output phase and power of every TR module of the EAR is kept equal, to an accuracy of  $7^\circ$  and 0.2 dB. Considering that amplitude and phase errors are generally distributed randomly among the TR modules, there is no significant error in gain and direction of the main beam, while the

low-elevation sidelobes increase in proportion to the magnitudes of the errors.

[46] A two-way array pattern in a plane which contains the Moon orbit was measured during passage of the Moon. The measurement was conducted during a one-hour period from 1515 to 1615 LT on 27 April 2001. The beam was fixed to  $22.8^\circ$  in zenith and  $351.9^\circ$  in azimuth where the apparent velocity of the Moon relative to the EAR on the Earth became zero at 1544 LT. A  $256\text{-}\mu\text{s}$  pulse was transmitted with an IPP of 5.2 ms. The echoes were over-sampled at 256 points with 2.4-km interval. No coherent integration was performed. Then 512-point complex FFTs were calculated in real time to obtain Doppler spectra every 2.7 s. The resultant power spectra were averaged for approximately 30 s. Since the distance between the EAR and the Moon surface is about 368,000 km, we do not receive any echoes from the moon during the first 2.45 s but we do receive range-aliased echoes afterward. The antenna pattern was obtained by choosing the peak value of the spectrum at the range of the maximum echo power of each 30-s data set and plotting it versus time (or corresponding azimuth angle).

[47] Figure 10 shows a cross section of the measured (solid curve) and the theoretical (dashed curve) relative gains of the EAR approximately in the east-west direction. Both the measured direction and gain of the main beam are in close agreement with theoretical values. The signal-to-noise ratio exceeded 15 dB. Consequently, the fluctuations of the measured values are thought not to be produced by noise fluctuations but by ionospheric scintillations, which have been found to be active during

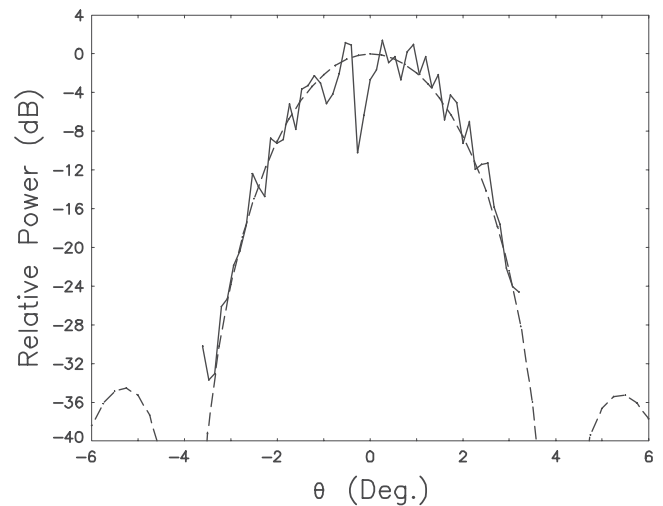


**Figure 10.** Relative gain of the EAR two-way antenna pattern (solid curve) measured by receiving Moon reflection echoes and the corresponding theoretical gain (dashed curve). The antenna beam is directed  $22.8^\circ$  from zenith and  $351.9^\circ$  in azimuth.

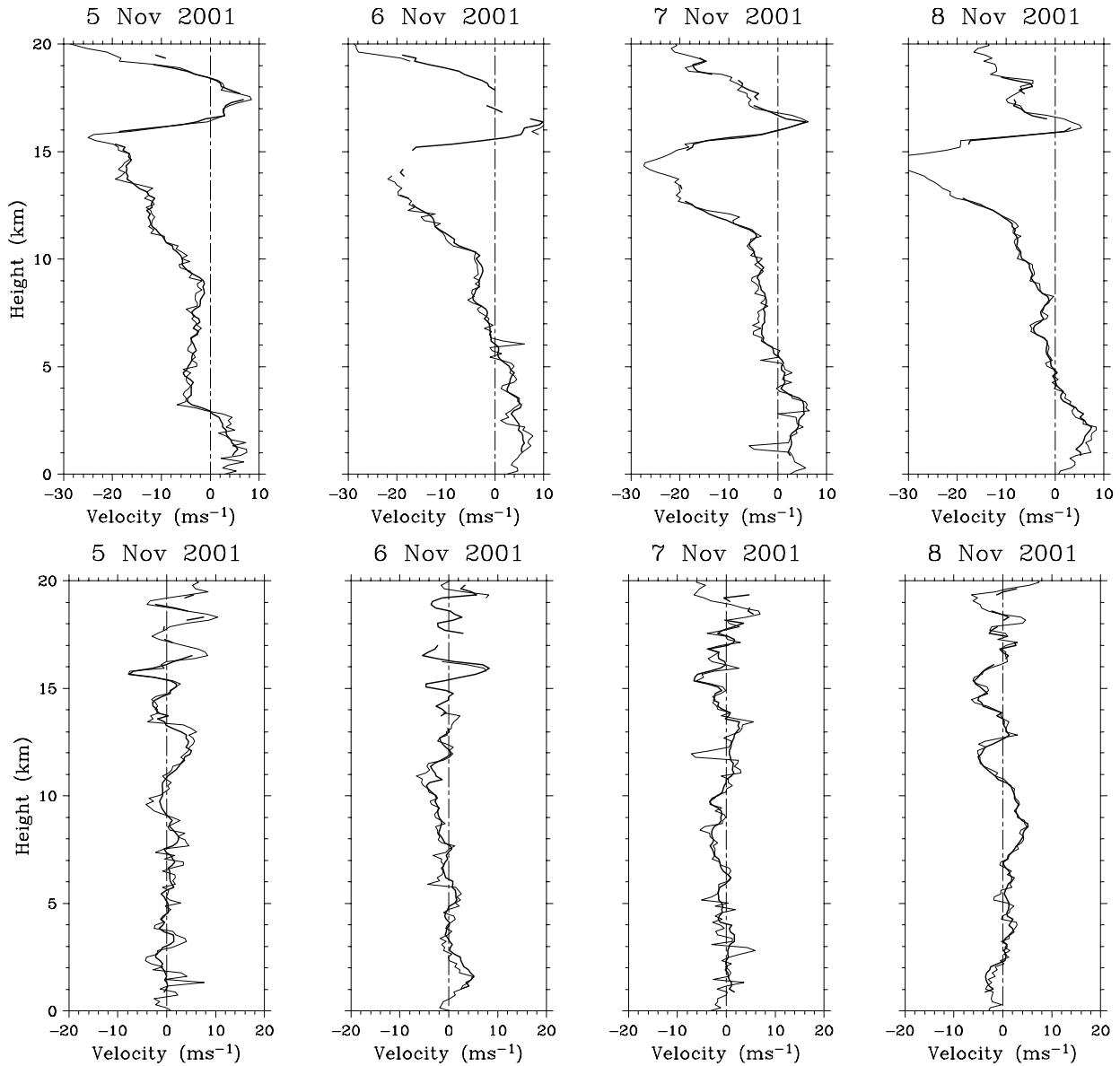


**Figure 11.** Zonal (upper panel; westerly or eastward positive) and meridional (lower panel; southerly or northward positive) wind profiles observed simultaneously with the EAR (thick curves) and GPS radiosondes (thin curves) around 13 LT on 5–8 November 2001. Height from the antenna field of the EAR is indicated.

equinoctial seasons over Sumatra in Indonesia. On the other hand, information on the sidelobes is not available due to limited sensitivity.

### 5.3. Simultaneous Wind Measurements of EAR With GPS Radiosondes

[48] Because of uncertainties in absolute range and echo direction from system biases and scattering characteristics, it is important to validate wind profiles obtained

by the EAR with other wind-measuring techniques. For this purpose we compared EAR wind profiles with those obtained simultaneously with GPS rawinsondes in November 2001. More than 170 GPS radiosondes were launched from the radar site every 3 or 6 hours by the Frontier Observation Research System for Global Change of Japan.

[49] The beam of the EAR was steered to five directions (vertical, and north, south, east, and west) every

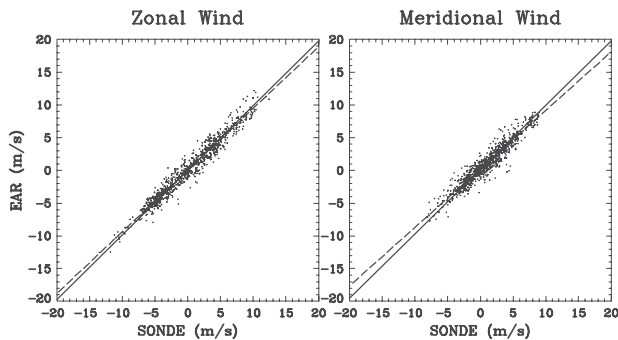


**Figure 12.** Scatterplots of zonal (left panel) and meridional (right panel) wind velocities observed below 10 km altitude with the EAR and radiosondes from 1 to 28 November 2001. Best fit linear-regression lines are shown, for both the regression of rawinsonde data on the radar data (solid line), and vice versa (dotted line).

IPP (400  $\mu$ s). We chose a zenith angle of  $10^\circ$  because it has been used for routine observations of the troposphere and the lower stratosphere with the MU radar since 1986 and repeated validations of those measured winds have been made with radiosonde measurements [e.g., Luce *et al.*, 2001a]. A 16-bit optimal code with a subpulse width of 1  $\mu$ s was used. The data were sampled at 150 ranges with 150-m intervals and coherent integration was performed 32 times. Then 256-point complex FFTs were calculated in real time to obtain Doppler spectra every 16.4 s. The resultant power spectra were averaged for approximately 80 s.

[50] Figure 11 compares the altitude profiles of wind velocities obtained by the EAR with those obtained with the GPS radiosondes launched around 13 LT on 5–8 November 2001. The EAR data were averaged for one hour around the rawinsonde launch time. The wind profiles are in good agreement in the altitude range of 1 to 20 km, although some EAR data are missing below the tropopause region, 15–17 km, due to low signal-to-noise ratios that are commonly encountered by 50-MHz atmospheric radars with similar sensitivities [Hocking, 1997].

[51] Figure 12 shows scatterplots of horizontal winds obtained with the EAR and radiosondes during the entire month of November 2001. All data in the altitude range from 1.5 to 10 km, where effective data were obtained with both instruments, are utilized. The wind velocities are in good agreement, obtaining correlation coefficients of 0.98 (zonal) and 0.95 (meridional). Best fit linear-regression lines are shown, for both regression of rawinsonde data on radar data (i.e., zero error is assumed in the radar data; solid line) and vice versa (i.e., zero error is assumed in the rawinsonde data; dotted line). The small differences seen may be plausibly attributed to errors

associated with both radar and rawinsonde measurements [Hocking, 2001]. However, the random error of horizontal winds measured by radars with a good detectability is estimated to be about  $0.7 \text{ ms}^{-1}$  [Yamamoto *et al.*, 1988]. This value is substantially smaller than the scatter of the data points in Figure 12. This result demonstrates the validity of EAR wind measurements, although further investigation may be needed regarding effects of partial reflection.

## 6. Preliminary Observational Results

### 6.1. Atmospheric Observations

[52] The EAR is the first radar in equatorial regions to make observations with a resolution as fine as 75–150 m. Radars in the Trans-Pacific Profiler Network (TPPN) operated by NOAA use range resolutions of approximately 1 km. The Gadanki radar in India ( $13.5^\circ\text{N}$ ,  $79.2^\circ\text{E}$ ) has a resolution of 150 m [Rao *et al.*, 1995], but it is located far from the equator. The EAR has been in full continuous operation since 1 July 2001, with only occasional interruptions to repair and maintain hardware and software.

[53] Figure 13 shows an altitude-time intensity plot of one-hour averages of atmospheric echoes observed with the EAR from July to late December in 2001. The short data gaps were caused mainly by commercial electric-power failures, which the EAR engine generator could not successfully compensate for. The echo intensity was weaker from late August to late October than in other

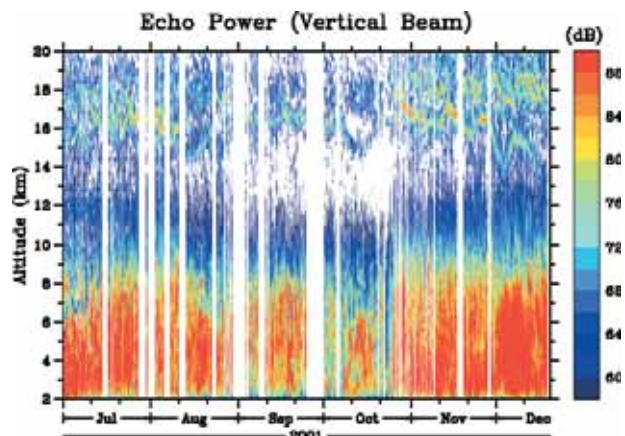


**Figure 13.** Altitude-time intensity plot of echo power observed in the vertical beam of the EAR from July to December 2001. The echo power is given in arbitrary units. The echo power is about 8 dB weaker from late August to late October than in other periods because of trouble with the preamplifier (Pre-amp).

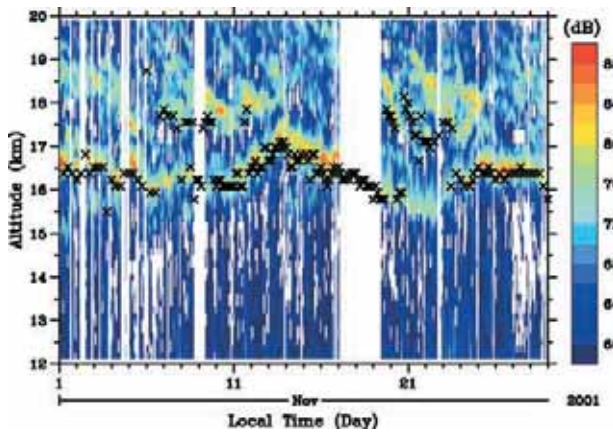


**Figure 14.** Altitude-time intensity plot of echo power observed in the vertical beam of the EAR during 1–28 November 2001. The cold-point tropopause defined by GPS rawinsonde measurements is indicated by crosses.

periods because of initial trouble with the band-pass filter in the preamplifier (Pre-amp).

[54] We note that multiple layers of intense radar echoes appear in the plot at altitudes between 15 and 19 km. The lowest layer usually corresponds in altitude with the minimum temperature (or the cold-point tropopause) observed with the GPS radiosondes. However, when the cold-point tropopause is occasionally displaced to a higher altitude (as determined from rawinsonde data), radar echoes sometimes continue to be observed from the original tropopause altitude, while additional echoes appear at the new tropopause location, as seen during 7–9 and 20–23 November (see Figure 14). A possible interpretation would be in terms of local temperature minima produced by the presence of Kelvin waves that are known to be active above the tropopause [e.g., *Andrews et al.*, 1987].

[55] On the other hand, the echo intensity, especially below 10 km, varies considerably with altitude and time due primarily to changes in humidity. This feature seems to be associated with cloud activity inferred from the images of the GMS (Geostationary Meteorological Satellite). More detailed discussion will be left to subsequent papers.

[56] Figure 15 shows altitude-time intensity plots of the vertical, zonal, and meridional components of the wind averaged over one hour during the same period. Short-period fluctuations due to buoyancy waves, with periods of less than a day, are more dominant in the vertical wind than in the horizontal wind, similar to cases observed at middle and high latitudes.

[57] In the troposphere the westerlies (eastward wind) are dominant below 10 km while the easterlies (westward wind) are dominant above that altitude. Although not yet

well understood, the observed zonal wind varies with periods from 30 to 60 days below 10 km, and seems to be associated with the Madden-Julian Oscillation (MJO) [*Madden and Julian*, 1994]. Strong vertical shear in the zonal wind accompanied by an intense echo layer near the cold-point tropopause is also observed. Recurring downward phase progression with periods of approximately 10 days above the cold-point tropopause is associated with Kelvin waves [*Fujiwara et al.*, 2003].

[58] On the other hand, shorter-period fluctuations are dominant in the meridional wind in both the troposphere (approximately 10 days) and lower stratosphere (4–5 days). These may be mixed Rossby-gravity waves [*Yanai and Maruyama*, 1966; *Wheeler and Kiladis*, 1999; *Widiyatmi et al.*, 1999, 2001].

[59] Changes in the vertical structure of atmospheric waves and turbulence over Sumatra, associated with

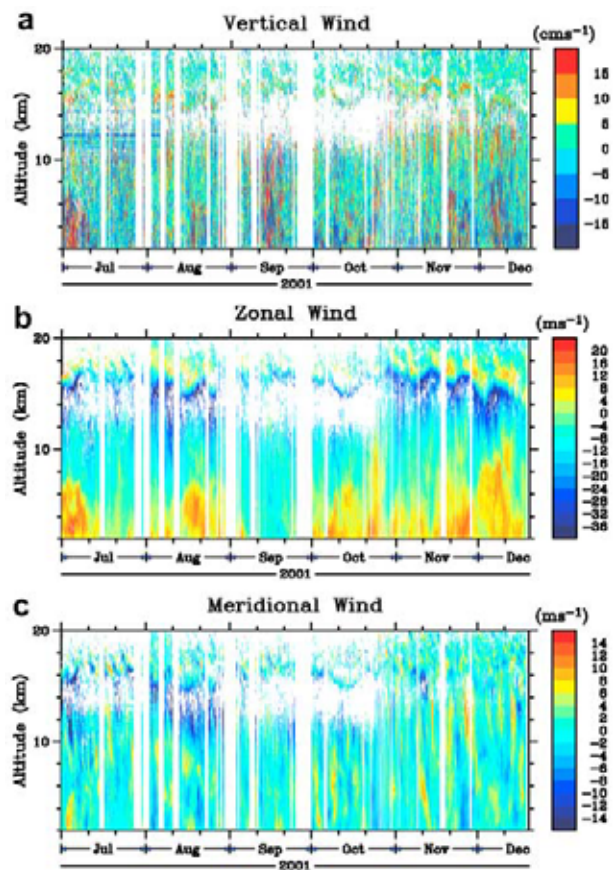


**Figure 15.** Altitude-time intensity plots of vertical (top panel), zonal (middle panel), and meridional (bottom panel) winds observed with the EAR from July to December 2001. Positive values indicate updraft, westerly (eastward), and southerly (northward) winds.

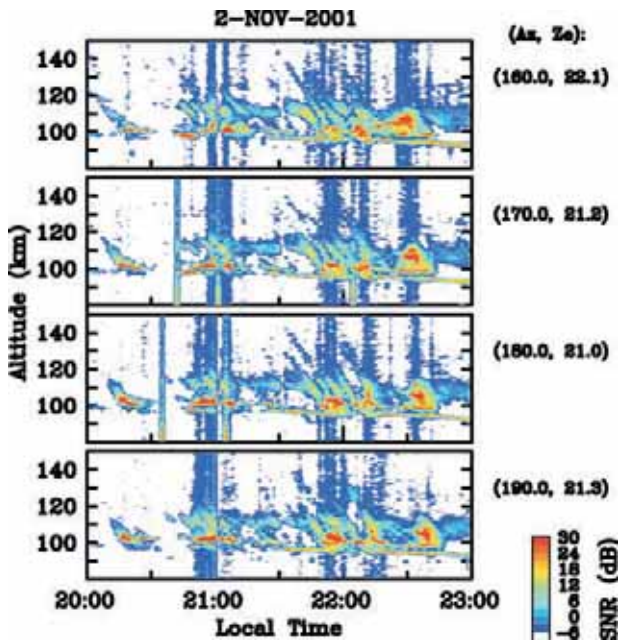


Figure 16. Altitude-time plots of FAI echo intensity in four directions near due south perpendicular to the geomagnetic field in the *E* region on 2 November 2001.

MJO and possible changes of MJO due to the Sumatra mountain ridge [Murata *et al.*, 2002], will be investigated with the EAR in the future. Also, it will be interesting to study effects of El Niño and La Niña on dynamics over Sumatra with the EAR.

### 6.2. Ionospheric Observations

[60] The MU radar has been shown to be fully capable of operating as a “coherent scatter” radar, and intensive efforts have been dedicated to the understanding of 3-m-scale field-aligned irregularities (FAIs) at midlatitudes [e.g., Fukao *et al.*, 1988, 1991; Yamamoto *et al.*, 1991, 1992, 1994]. The EAR is a similar VHF radar which is also capable of viewing the ionosphere in directions perpendicular to the geomagnetic field, but it is the first one established in the geomagnetic southern hemisphere (10.63°S, 171.93°E). It is located in altitude outside of the equatorial electrojet (EEJ) but within the equatorial (or Appleton) anomaly region.

[61] The EAR has been applied to study *F* region FAIs associated with equatorial spread *F* (ESF) from nearly 10°S (geomagnetic latitude). Such studies have been conducted extensively by the Jicamarca radar at the geomagnetic equator in South America [e.g., Woodman and Hoz, 1976]. The EAR has also been utilized for observations of *E* region FAIs in regions outside the EEJ, where their characteristics are not well known because

only a few such radar observations have been made [e.g., Woodman *et al.*, 1999; Chau and Woodman, 1999; Choudhary *et al.*, 1996; Patra *et al.*, 2002].

[62] Figure 16 shows altitude-time-intensity plots of FAI echo power from the *E* region in four beam directions near due south: (160.0°, 22.1°), (170.0°, 21.2°), (180.0°, 21.0°), and (190.0°, 21.3°) in azimuth and zenith, respectively. A single pulse of 4-μs width (or 600 m range resolution) was used. The condition of perpendicularity to the geomagnetic field for the 3.4° antenna beam width is satisfied over the entire altitude range 80 to 150 km. The echoes appear extended in altitude, from 95 to 140 km, and the maximum echo intensity is more than 35 dB larger than the noise level. Features similar to those reported for other locations are commonly observed above 100 km: Quasi-periodic striations, downward (toward the radar) progression of echo regions, and relatively wide spectral widths. The unique capability of the EAR to observe in different directions simultaneously will help investigation of the spatial structure and movements of FAIs. For instance, some echoes occur almost simultaneously in the four

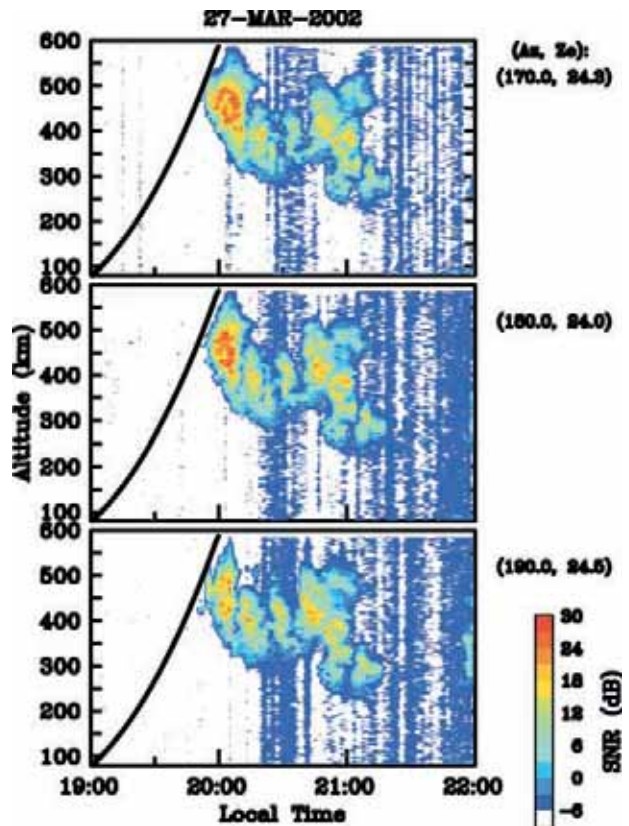
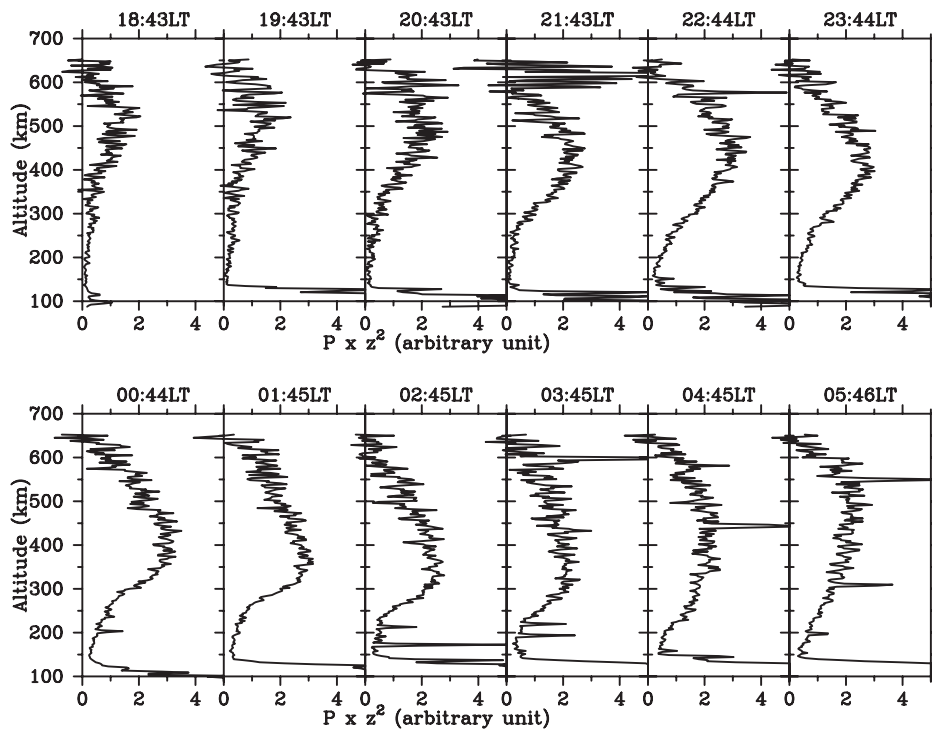


Figure 17. As for Figure 16, but for the *F* region on 27 March 2002. The black line shows the solar terminator.



**Figure 18.** Altitude profiles of incoherent scatter echo intensity observed with the EAR from 1843 LT on 7 November 2001 to 0545 LT on the following day. The echo intensity is given in arbitrary linear units with range divergence compensated.

beam directions, while others show westward propagation with a phase velocity of 15 to 20  $\text{ms}^{-1}$ , as observed at midlatitudes.

[63] Intense FAI echoes have also been observed over a wide altitude range in the nighttime  $F$  region, as shown in Figure 17. A 13-bit Barker-coded pulse with a 16- $\mu\text{s}$  subpulse (or 2.4 km range resolution) was used. The time resolution is 62 s. The radial drift velocities are usually less than 100  $\text{ms}^{-1}$  but occasionally exceed 200  $\text{ms}^{-1}$ . Upward-developing plumes and upwelling of the bottom-side  $F$  layer, commonly associated with ESF [Tsunoda and White, 1981] have been detected also with the EAR near 10°S, as well as with the Gadanki radar at 6.3°N [Rao *et al.*, 1997]. These results will be discussed elsewhere.

[64] As mentioned above, the EAR is approximately 10 dB less sensitive than the MU radar. However, the ionospheric density is, at least, two-to-three times larger in the equatorial anomaly than at midlatitudes [e.g., Rishbeth and Garriott, 1969], and the very weak incoherent scattering (IS) originating from the free electrons is also detectable with the EAR [Sato *et al.*, 1989]. A preliminary measurement of the IS power profile has already been made using a 7-bit Barker coded pulse of 224- $\mu\text{s}$  width (7 bits  $\times$  32  $\mu\text{s}$ ).

[65] Figure 18 shows a sequence of such profiles obtained from 1843 LT on 7 November 2001 to 0545 LT on the following day. The beam was directed, sequentially, with a 10° zenith angle toward the north, east, south, and west on a pulse-to-pulse basis, and the profiles shown are averages of the four beams. The observation was made in a one-hour cycle changing sequentially between five different modes. The IS power-profile mode was operated for approximately 10 min each hour. The feature of the electron density profile that is typical of the low-latitude ionosphere is the high  $F$  layer peak in the evening followed by a subsequent lowering of the layer toward midnight. Fluctuations with vertical scale of 10 to 15 km are seen in the echo power profile. This is consistent with altitude fluctuations caused by Faraday rotation, estimated with electron density profiles from the International Reference Ionosphere [Bilitza, 1997].

[66] Multipulse transmission capability, similar to that used with the MU radar [Sato *et al.*, 1989], will be implemented in the near future for spectral measurements to observe  $F$  region temperature, drift velocity, and electron density as well. Also, it is noted that the geomagnetic conjugate point of the EAR is 16.69°N and 100.17°E, north of Bangkok, Thailand, that will provide

unique convenience for conjugate point observations with an ionosonde, an airglow imager, etc., in the future.

## 7. Concluding Remarks

[67] In this paper we have described the EAR recently installed at the Indonesian equator (0.20°S, 100.32°E; geomagnetic latitude 10.63°S). The EAR is a 47-MHz Doppler radar with an active phased-array system. The system is composed of 560 three-element Yagi antennas and an equivalent number of solid state power amplifiers (TR modules). The nominal beam width is 3.4° while the nominal peak and maximum average radiation powers are 100 kW and 5 kW, respectively.

[68] The antenna pattern of the EAR has been favorably calibrated by using emissions from Cygnus-A and reflections from the Moon. Also, we have presented the results of simultaneous wind observations with GPS radiosondes. These results have demonstrated the EAR as a reliable tool for observing wind profiles in the troposphere and lower stratosphere and 3-m scale field-aligned irregularities (FAIs) in the ionosphere over the Indonesian Archipelago.

[69] The EAR is now being continuously operated and provides valuable data day by day. High-resolution observations with the EAR, never before realized, must play an important role in various studies of the equatorial atmosphere and ionosphere. It is expected that the EAR will be operated in collaboration with other existing networks of radars, such as those mentioned in the Introduction, satellites such as TIMED (Thermosphere Ionosphere Mesosphere Energetics and Dynamics) of the USA and ROCSAT-1 of the Republic of China (Taiwan) [Su *et al.*, 2001], and other ground-based radio and optical sensors. The EAR is expected to proceed to study the hierarchical structure of atmospheric variations in the equatorial region using the data from these instruments in the future.

[70] **Acknowledgments.** The authors are indebted to the National Institute of Aeronautics and Space of Indonesia (LAPAN) for their collaboration. Thanks are also due to colleagues of the Agency for the Assessment and Application of Technology (BPPT) of Indonesia, the Agency of Meteorology and Geophysics (BMG) of Indonesia and the Radio Science Center for Space and Atmosphere of Kyoto University (RASC) for their continuing support. We thank M.-D. Yamana, S. Mori, and J. Hamada of the Frontier Observation Research System for Global Change of Japan for providing the GPS radiosonde data. Some of the preliminary observations presented in the paper were conducted in collaboration with H. Luce (RASC), Y. Otsuka (Solar-Terrestrial Environment Laboratory, Nagoya University), and A. Saito (Geophysical Institute, Kyoto University), and we are grateful to them. T. Horinouchi and M. Fujiwara (RASC) are also acknowledged for their valuable comments in regard to the data analysis. We thank R. T. Tsunoda (SRI International) for careful reading of

the original manuscript and W. L. Oliver (Boston University) for editing of its revised version. The authors express their gratitude to I. Hirota, Professor Emeritus of Kyoto University, for his continuing encouragement. Special thanks are due to S. Kato, Professor Emeritus of Kyoto University, for his advice and support. This project is partially supported by Grant-in-Aid for Scientific Research on Priority Area-764 of the Ministry of Education, Culture, Sports, Science and Technology of Japan. The operation of EAR is based upon the agreement between RASC and LAPAN signed on 8 September 2000.

## References

- Andrews, D. G., J. R. Holton, and C. B. Leovy, *Middle Atmosphere Dynamics, Int. Geophys. Ser.*, vol. 40, Academic, San Diego, Calif., 1987.
- Bilitza, D., International Reference Ionosphere—Status 1995/96, *Adv. Space Res.*, 20, 1751–1754, 1997.
- Chau, J. L., and R. F. Woodman, Low-latitude quasiperiodic echoes observed with the Piura VHF radar in the E region, *Geophys. Res. Lett.*, 26, 2167–2170, 1999.
- Choudhary, R. K., K. K. Mahajan, S. Singh, K. Kumar, and V. K. Anandan, First VHF radar observations of tropical latitude *fs*-region field aligned irregularities, *Geophys. Res. Lett.*, 23, 3683–3686, 1996.
- Czechowsky, P., G. Schmidt, and R. Rüster, The mobile SOUSY Doppler radar: Technical design and first results, *Radio Sci.*, 19, 441–450, 1984.
- Fejer, B. G., and M. C. Kelley, Ionospheric irregularities, *Rev. Geophys.*, 18, 401–454, 1980.
- Fujiwara, M., M. K. Yamamoto, H. Hashiguchi, T. Horinouchi, and S. Fukao, Turbulence at the tropopause due to breaking Kelvin waves observed by the Equatorial Atmosphere Radar, *Geophys. Res. Lett.*, 30(4), 1171, doi:10.1029/2002GL016278, 2003.
- Fukao, S., T. Sato, T. Tsuda, S. Kato, K. Wakasugi, and T. Makihira, The MU radar with an active phased array system: 1. Antenna and power amplifiers, *Radio Sci.*, 20, 1155–1168, 1985a.
- Fukao, S., T. Tsuda, T. Sato, S. Kato, K. Wakasugi, and T. Makihira, The MU radar with an active phased array system: 2. In-house equipment, *Radio Sci.*, 20, 1169–1176, 1985b.
- Fukao, S., T. Sato, and S. Kato, Monitoring of the MU radar antenna pattern by satellite OHZORA (EXOS-C), *J. Geomagn. Geoelectr.*, 37, 431–441, 1985c.
- Fukao, S., J. P. McClure, A. Ito, T. Sato, I. Kimura, T. Tsuda, and S. Kato, First VHF radar observation of midlatitude F-region field-aligned irregularities, *Geophys. Res. Lett.*, 15, 768–771, 1988.
- Fukao, S., T. Sato, T. Tsuda, M. Yamamoto, M. D. Yamanaka, and S. Kato, MU radar: New capabilities and system calibrations, *Radio Sci.*, 25, 477–485, 1990.
- Fukao, S., M. C. Kelley, T. Shirakawa, T. Takami, M. Yamamoto, T. Tsuda, and S. Kato, Turbulent upwelling of the midlatitude ionosphere: 1. Observational results by the MU radar, *J. Geophys. Res.*, 96, 3725–3746, 1991.

- Gage, K. S., B. B. Balsley, W. L. Ecklund, D. A. Carter, and J. R. McAfee, Wind profiler-related research in the tropical Pacific, *J. Geophys. Res.*, *96*, 3209–3220, 1991.
- Guidice, D. A., and J. P. Castelli, The use of extraterrestrial radio sources in the measurement of antenna parameters, *IEEE Trans. Aerosp. Electron. Syst.*, *7*, 226–234, 1971.
- Hashiguchi, H., S. Fukao, T. Tsuda, M. D. Yamanaka, D. L. Tobing, T. Sribimawati, S. W. B. Harijono, and H. Wiryo-sumarto, Observations of the planetary boundary layer over equatorial Indonesia with an L-band clear-air Doppler radar: Initial results, *Radio Sci.*, *30*, 1043–1054, 1995.
- Hocking, W. K., Recent advances in radar instrumentation and techniques for studies of the mesosphere, stratosphere, and troposphere, *Radio Sci.*, *32*, 2241–2270, 1997.
- Hocking, W. K., VHF tropospheric scatterer anisotropy at Resolute Bay and its implications for tropospheric radar-derived wind accuracies, *Radio Sci.*, *36*, 1777–1793, 2001.
- Kudeki, E., and F. R. Stitt, Frequency domain interferometry: A high resolution radar technique for studies of atmospheric turbulence, *Geophys. Res. Lett.*, *14*, 198–201, 1987.
- Luce, H., S. Fukao, M. Yamamoto, C. Sidi, and F. Dalaudier, Validation of winds measured by MU radar with GPS radiosondes during the MUTSI campaign, *J. Atmos. Oceanic Technol.*, *18*, 817–829, 2001a.
- Luce, H., M. Yamamoto, S. Fukao, D. Helal, and M. Crochet, A frequency radar interferometric imaging applied with high resolution methods, *J. Atmos. Sol. Terr. Phys.*, *63*, 221–234, 2001b.
- Madden, R. A., and P. R. Julian, Observations of the 40–50-day tropical oscillation—A review, *Mon. Weather Rev.*, *122*, 814–837, 1994.
- Maeda, K., H. Alvarez, J. Aparici, J. May, and P. Reich, A 45-MHz continuum survey of the northern hemisphere, *Astron. Astrophys.*, *140*, 145–154, 1999.
- Marshall, J. M., A. M. Peterson, and A. A. Barnes Jr. Combined radar-acoustic sounding system, *Appl. Opt.*, *11*, 108–112, 1972.
- Murata, F., M. D. Yamanaka, M. Fujiwara, S. Ogino, H. Hashiguchi, S. Fukao, M. Kudsy, T. Sribimawati, S. W. B. Harijono, and E. Kelena, Relationship between wind and precipitation observed with UHF radar, GPS rawinsondes and surface meteorological instruments at Kototabang, West Sumatera during September–October 1998, *J. Meteorol. Soc. Jpn.*, *80*, 347–360, 2002.
- Nakazawa, T., Tropical super clusters within intraseasonal variations over the western Pacific, *J. Meteorol. Soc. Jpn.*, *66*, 823–839, 1988.
- Palmer, R. D., T. Y. Yu, and P. B. Chilson, Range imaging using frequency diversity, *Radio Sci.*, *34*, 1485–1496, 1999.
- Patra, A. K., P. B. Rao, V. K. Anandan, A. R. Jain, and G. Viswanathan, Evidence of intermediate layer characteristics in the Gadanki radar observations of the upper E region field-aligned irregularities, *Geophys. Res. Lett.*, *29*(14), doi:10.1029/2001GL013773, 2002.
- Rao, P. B., A. R. Jain, P. Kishore, P. Balamuralidhar, S. H. Damle, and G. Viswanathan, Indian MST radar: 1. System description and sample vector wind measurements in ST mode, *Radio Sci.*, *30*, 1125–1138, 1995.
- Rao, P. B., A. K. Patra, T. V. Chandrasekhar Sarma, B. V. Krishna Marthy, K. S. V. Subba Rao, and S. S. Hari, Radar observations of updrafting and downdrafting plasma depletions associated with the equatorial spread F, *Radio Sci.*, *32*, 1215–1227, 1997.
- Renggono, F., et al., Precipitating clouds observed by L-band boundary layer radars in equatorial Indonesia, *Ann. Geophys.*, *19*, 889–897, 2001.
- Rishbeth, H., and O. K. Garriott, *Introduction to Ionospheric Physics*, *Int. Geophys. Ser.*, vol. 14, Academic, San Diego, Calif., 1969.
- Sato, T., A. Ito, W. L. Oliver, S. Fukao, T. Tsuda, S. Kato, and I. Kimura, Ionospheric incoherent scatter measurements with the middle and upper atmosphere radar: Techniques and capability, *Radio Sci.*, *24*, 85–98, 1989.
- Schmidt, G., R. Rüster, and P. Czechowsky, Complementary code and digital filtering for detection of weak VHF radar signals from the mesosphere, *IEEE Trans. Geosci. Electron.*, *17*, 154–161, 1979.
- Smaini, L., H. Luce, M. Crochet, and S. Fukao, An improved high-resolution processing method for a frequency domain interferometric imaging (FII) technique, *J. Atmos. Oceanic Technol.*, *19*, 954–966, 2002.
- Spano, E., and O. Ghebrehbrhan, Pulse coding techniques for ST/MST radar systems: A general approach based on a matrix formulation, *IEEE Trans. Geosci. Remote Sens.*, *34*, 304–316, 1996a.
- Spano, E., and O. Ghebrehbrhan, Complementary sequences with high sidelobe suppression factors for ST/MST radar applications, *IEEE Trans. Geosci. Remote Sens.*, *34*, 317–329, 1996b.
- Spano, E., and O. Ghebrehbrhan, Sequences of complementary codes for the optimum decoding of truncated ranges and high sidelobe suppression factors for ST/MST radar systems, *IEEE Trans. Geosci. Remote Sens.*, *34*, 330–345, 1996c.
- Su, S.-Y., H. C. Yeh, and R. A. Heelis, ROCSAT 1 ionospheric plasma and electrodynamics instrument observations of equatorial spread F: An early transitional scale result, *J. Geophys. Res.*, *106*, 29,153–29,159, 2001.
- Tsuda, T., T. Adachi, Y. Masuda, S. Fukao, and S. Kato, Observations of tropospheric temperature fluctuations with the MU radar-RASS, *J. Atmos. Oceanic Technol.*, *11*, 50–64, 1994.
- Tsunoda, R. T., and B. R. White, On the generation and growth of equatorial backscatter plumes: 1. Wave structure in the bottomside F layer, *J. Geophys. Res.*, *86*, 3610–3616, 1981.
- Wheeler, M., and G. N. Kiladis, Convectively coupled equatorial waves: Analysis of clouds and temperature in the wave-number-frequency domain, *J. Atmos. Sci.*, *56*, 374–399, 1999.

- Widiyatmi, I., M. D. Yamanaka, H. Hashiguchi, S. Fukao, T. Tsuda, S. Ogino, S. W. B. Harijono, and H. Wiryosumarto, Quasi 4 day mode observed by a boundary layer radar at Serpong (6°S, 107°E), Indonesia, *J. Meteorol. Soc. Jpn.*, *77*, 1177–1184, 1999.
- Widiyatmi, I., H. Hashiguchi, S. Fukao, M. D. Yamanaka, S.-Y. Ogino, K. S. Gage, S. W. B. Harijono, S. Diharto, and H. Djojodihardjo, Examination of 3–6 day disturbances over equatorial Indonesia based on boundary layer radar observations during 1996–1999 at Bukittinggi, Serpong and Biak, *J. Meteorol. Soc. Jpn.*, *79*, 317–331, 2001.
- Woodman, R. F., High-altitude resolution stratospheric measurements with the Arecibo 430-MHz radar, *Radio Sci.*, *15*, 423–430, 1980.
- Woodman, R. F., and C. L. Hoz, Radar observations of *F* region equatorial irregularities, *J. Geophys. Res.*, *81*, 5447–5466, 1976.
- Woodman, R. F., J. L. Chau, and F. Aquino, Low-latitude field aligned irregularities observed in the E region with the Piura VHF radar: First results, *Radio Sci.*, *34*, 983–990, 1999.
- Worthington, R. M., R. D. Palmer, and S. Fukao, An investigation of tilted aspect-sensitive scatterers in the lower atmosphere using the MU and Aberystwyth VHF radars, *Radio Sci.*, *34*, 413–426, 1999.
- Yamamoto, M., T. Sato, P. T. May, T. Tsuda, S. Fukao, and S. Kato, Estimation error of spectral parameters of mesosphere-stratosphere-troposphere radars obtained by least squares fitting methods and its lower bound, *Radio Sci.*, *23*, 1013–1021, 1988.
- Yamamoto, M., S. Fukao, R. F. Woodman, T. Ogawa, T. Tsuda, and S. Kato, Midlatitude *E*-region field-aligned irregularities observed with the MU radar, *J. Geophys. Res.*, *96*, 15,943–15,949, 1991.
- Yamamoto, M., S. Fukao, T. Ogawa, T. Tsuda, and S. Kato, A morphological study on mid-latitude *E*-region field-aligned irregularities observed with the MU radar, *J. Atmos. Terr. Phys.*, *54*, 769–777, 1992.
- Yamamoto, M., N. Komoda, S. Fukao, R. T. Tsunoda, T. Ogawa, and T. Tsuda, Spatial structure of the *E*-region field-aligned irregularities revealed by the MU radar, *Radio Sci.*, *29*, 337–347, 1994.
- Yanai, M., and T. Maruyama, Stratospheric wave disturbances propagating over the equatorial Pacific, *J. Meteorol. Soc. Jpn.*, *44*, 291–294, 1966.
- 
- S. Fukao, H. Hashiguchi, T. Nakamura, T. Tsuda, M. Yamamoto, and M. K. Yamamoto, Radio Science Center for Space and Atmosphere, Kyoto University, Uji, 611-0011 Kyoto, Japan. (hasiguti@kurasc.kyoto-u.ac.jp)
- M. Hagio and Y. Yabugaki, Communication Systems Center, Mitsubishi Electric Corporation, 8-1-1 Tsukaguchi-Honmachi, Amagasaki, 661-8661 Hyogo, Japan.
- T. Sato, Graduate School of Informatics, Kyoto University, Sakyo, 606-8501 Kyoto, Japan.